







## Magnetically tuned continuous transition from weak to strong coupling in terahertz magnon polaritons

Andrey Baydin <sup>1,2,\*</sup>, Kenji Hayashida,<sup>1,3</sup> Takuma Makihara,<sup>4</sup> Fuyang Tay <sup>1,5</sup>, Xiaoxuan Ma <sup>6</sup>, Wei Ren,<sup>6</sup> Guohong Ma,<sup>6</sup> G. Timothy Noe, II,<sup>1</sup> Ikufumi Katayama,<sup>7</sup> Jun Takeda <sup>7</sup>, Hiroyuki Nojiri,<sup>8</sup> Shixun Cao <sup>6,†</sup>, Motoaki Bamba,<sup>9,10,11</sup> and Junichiro Kono <sup>1,2,4,12,‡</sup>

<sup>1</sup>Department of Electrical and Computer Engineering, Rice University, Houston, Texas 77005, USA

<sup>2</sup>Smalley-Curl Institute, Rice University, Houston, Texas 77005, USA

<sup>3</sup>Division of Applied Physics, Graduate School of Engineering, Hokkaido University, Sapporo, Hokkaido 060-8628, Japan

<sup>4</sup>Department of Physics and Astronomy, Rice University, Houston, Texas 77005, USA

<sup>5</sup>Applied Physics Graduate Program, Smalley-Curl Institute, Rice University, Houston, Texas 77005, USA

<sup>6</sup>Department of Physics, International Center of Quantum and Molecular Structures and Materials Genome Institute, Shanghai University 200444, Shanghai, China

<sup>7</sup>Department of Physics, Graduate School of Engineering Science, Yokohama National University, Yokohama 240-8501, Japan

<sup>8</sup>Institute for Materials Research, Tohoku University, Sendai 980-8577, Japan

<sup>9</sup>The Hakubi Center for Advanced Research, Kyoto University, Kyoto 606-8502, Japan

<sup>10</sup>Department of Physics I, Kyoto University, Kyoto 606-8502, Japan

<sup>11</sup>PRESTO, Japan Science and Technology Agency, Kawaguchi 332-0012, Japan

<sup>12</sup>Department of Materials Science and NanoEngineering, Rice University, Houston, Texas 77005, USA



(Received 16 August 2022; revised 7 November 2022; accepted 24 February 2023; published 20 March 2023)

Depending on the relative rates of coupling and dissipation, a light-matter coupled system is either in the weak- or strong-coupling regime. Here, we present a unique system where the coupling rate continuously increases with an externally applied magnetic field while the dissipation rate remains constant, allowing us to monitor a weak-to-strong coupling transition as a function of magnetic field. We observed a Rabi splitting of a terahertz magnon mode in yttrium orthoferrite above a threshold magnetic field of  $\sim 14$  T. Based on a microscopic theoretical model, we show that with increasing magnetic field the magnons transition into magnon polaritons through an exceptional point, which will open up new opportunities for *in situ* control of non-Hermitian systems.

DOI: [10.1103/PhysRevResearch.5.L012039](https://doi.org/10.1103/PhysRevResearch.5.L012039)

Understanding and harnessing the interplay of driving and dissipation in open quantum systems is an important contemporary problem in technology and science. Many quantum technologies, including quantum computation, sensing, and transduction, are enabled by coherent light-matter coupling, but the coherence can be easily washed out when the matter interacts with dissipative environments. On the other hand, dissipation can be engineered for dissipative quantum error correction schemes as well as for stabilizing qubits against decoherence [1–4]. Further, driven-dissipative many-body systems can exhibit exotic nonequilibrium phenomena and phases [5–7].

In a strongly coupled light-matter system, the coupling rate  $g$  exceeds the rates of dissipation for light ( $\kappa$ ) and

matter ( $\gamma$ ), satisfying  $C = 4g^2/\kappa\gamma > 1$ , where  $C$  is called the cooperativity [8–10]. Typically, the matter is placed in a small-mode-volume photonic cavity to enhance  $g$ . Such cavity-quantum-electrodynamics systems have recently attracted much theoretical attention as controllable open quantum systems, in which the physics of exceptional points, non-Hermitian Hamiltonians, and parity-time symmetry can be explored [11–17]. In particular, exceptional points, which are spectral singularities where the eigenvalues and eigenvectors coalesce [18], are expected to be useful for manipulating light via nontrivial topological effects [19–21].

Experimentally, several physical platforms have shown a transition from the weak-coupling regime ( $C < 1$ ) to the strong-coupling regime ( $C > 1$ ), including intersubband polaritons in quantum wells through gating [22] or ultrafast optical excitation [23], microcavity exciton polaritons in aligned carbon nanotubes through polarization rotation [24], a metal–semiconductor hybrid resonator through spacer thickness variation [25], magnon-polaritons in yttrium iron garnet through position tuning inside a microwave cavity [26,27], and by controlling the relative phase and amplitude ratio between the cavity field and the corresponding field of a microwave drive [28]. Also, a transition from coherent to dissipative coupling has been observed by changing the magnon

\*baydin@rice.edu

†sxcao@shu.edu.cn

‡kono@rice.edu

dissipation rate [29,30]. However, continuous facile tuning of  $g$ ,  $\gamma$ , or  $\kappa$  by an external field in a single sample has not been achieved.

Here, we demonstrate *in situ* tuning of  $g$  by an external magnetic field ( $H$ ) for propagating bulk magnon-polaritons in the antiferromagnetic state of yttrium orthoferrite (YFeO<sub>3</sub>). We used single-shot terahertz (THz) time-domain spectroscopy [31,32] in high magnetic fields up to 30 T and observed a field-induced peak splitting of a THz magnon mode in YFeO<sub>3</sub>. The magnon peak in transmission spectra remains a single peak until a critical field ( $\sim 14$  T) is reached, where it splits into two, and the two-peak spectrum persists up to 30 T. Our microscopic model quantitatively explains the experimental data. The model shows that the coupling rate  $g$  continuously increases with increasing  $H$ , and exact coupling-dissipation compensation ( $C = 1$ ) occurs at the critical field, which is the exceptional point in this system. The magnitude of splitting also increased with increasing sample thickness, in proportion to the square root of the thickness.

The YFeO<sub>3</sub> samples we studied were  $c$ -cut single crystals grown in an optical floating zone furnace. The samples were elliptical plates of 6 mm  $\times$  4 mm with thicknesses of 1.5, 1.9, and 2.97 mm. The main results are presented for the 2.97-mm-thick sample. We performed THz magnetospectroscopy measurements on these samples using the Rice Advanced Magnet with Broadband Optics (RAMBO) [33], which combines single-shot THz detection and pulsed high magnetic fields up to 30 T [31] [see Fig. 1(a)]. Bursts of THz radiation were generated through optical rectification by passing the output beam of an amplified Ti:sapphire laser (1 kHz, 150 fs, 775 nm, 0.8 mJ, Clark-MXR, Inc., CPA-2001) through a LiNbO<sub>3</sub> crystal. We recorded the time-domain waveform of the THz pulses that transmitted through the sample by electro-optic sampling in ZnTe in a single-shot manner using a reflective echelon [31,32].

YFeO<sub>3</sub> is a canted antiferromagnet and hosts two magnon modes: the quasiferromagnetic (qFM) mode and the quasiantiferromagnetic (qAFM) mode. The spin motion of the qFM mode is depicted in Fig. 1(b), where  $\vec{S}_1$  and  $\vec{S}_2$  represent Fe<sup>3+</sup> spins in the two Fe sublattices, and  $\vec{M}$  is the net magnetization as a result of canting. In the present work, we were primarily interested in the coupling between the magnetic field component of the incident THz radiation,  $\vec{H}_{\text{THz}}$ , and the qFM mode. Figure 1(c) schematically shows the experimental configuration we employed. The two spins lie in the  $a$ - $c$  plane, which are shown by blue solid arrows. The Cartesian coordinates  $x$ ,  $y$ , and  $z$  are parallel to the crystal  $a$ ,  $b$ , and  $c$  axes, respectively. The electric field component of the incident THz radiation,  $\vec{E}_{\text{THz}}$ , was along the  $b$  axis, and the magnetic field component,  $\vec{H}_{\text{THz}}$ , was along the  $a$  axis, respectively. In this geometry, only the qFM mode can be excited through the Zeeman torque [34]. The external millisecond-long pulsed magnetic field generated by the RAMBO system was applied parallel to the  $c$  axis; it was essentially constant for the duration of the picosecond-long THz pulse, and therefore, it can be safely considered to be a dc magnetic field,  $\vec{H}_{\text{dc}}$ , shown by a black arrow.

Figure 2(a) shows a series of time-domain traces of THz electric fields transmitted through the sample at various selected dc magnetic fields from 9.2 to 26.6 T. For

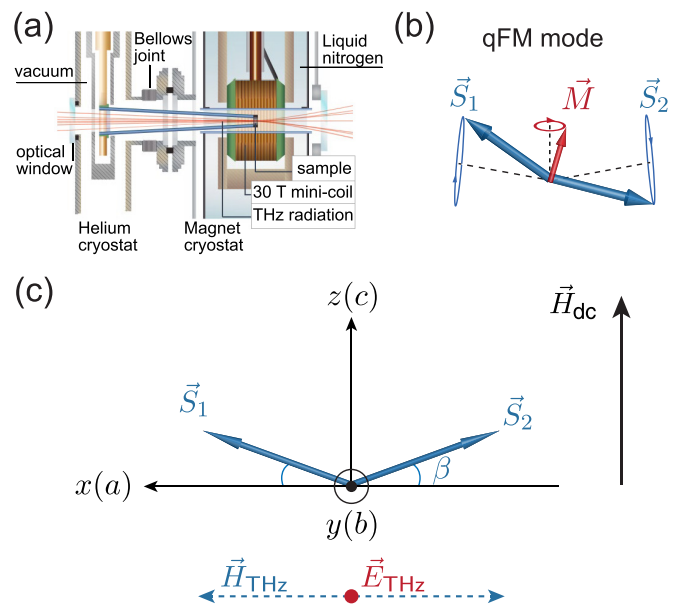


FIG. 1. (a) Schematic of the experimental setup, showing a table-top minicoil pulse magnet with optical access (RAMBO). (b) Spin motion of the quasiferromagnetic (qFM) magnon mode in YFeO<sub>3</sub>.  $\vec{S}_1$  and  $\vec{S}_2$  are spins in the two respective sublattices with a small canting angle, which produces a net magnetization  $\vec{M}$ . (c) Experimental geometry. The two sublattice spins lie in the  $a$ - $c$  plane with a canting angle  $\beta$ . The Cartesian coordinates,  $x$ ,  $y$ , and  $z$ , are parallel to the crystal  $a$ ,  $b$ , and  $c$  axes, respectively. The electric (magnetic) field component of the THz radiation,  $\vec{E}_{\text{THz}}$  ( $\vec{H}_{\text{THz}}$ ), was parallel to the  $b$  axis ( $a$  axis). The black arrow on the right shows the external millimeter-long pulsed magnetic field produced by the RAMBO magnet, which can be considered to be a dc field  $\vec{H}_{\text{dc}}$ , during the picosecond-long THz pulse. In this configuration, only the qFM mode is excited through the Zeeman torque.

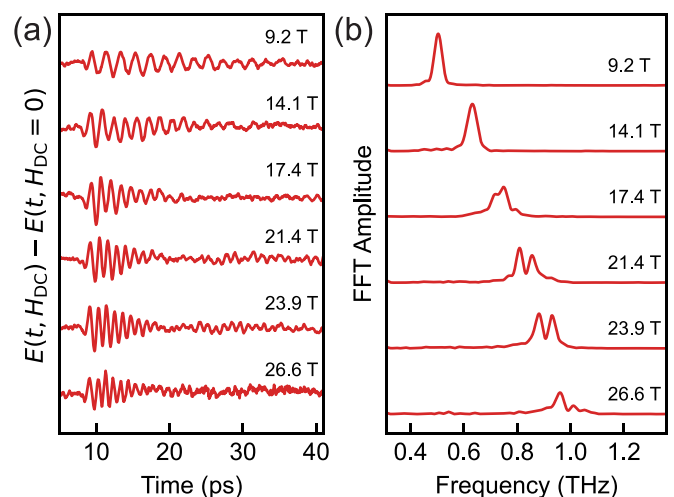


FIG. 2. (a) Magnetic-field-induced changes in the transmitted THz electric field as a function of time at various magnetic fields from 9.2 to 26.6 T. (b) Fourier transforms of the time-domain waveforms in (a). The traces are vertically offset for clarity both in (a) and in (b).

each magnetic field, we subtracted the THz electric-field waveform at zero magnetic field,  $E_{\text{THz}}(t, H_{\text{dc}} = 0)$ , from the THz electric-field waveform recorded at the magnetic field,  $E_{\text{THz}}(t, H_{\text{dc}})$ . This differentiation procedure allows us to focus on the magnetic-field-induced changes in the material's THz response. At low magnetic fields ( $< 14$  T), we observe long-lived coherent oscillations, with monotonically decaying amplitude, due to the qFM magnon mode excited by the incident THz pulse, as expected for this configuration [35]. Above 14 T, however, the data start showing beating behavior, indicating the existence of two oscillation modes with different but similar frequencies. The corresponding Fourier transforms of the data into the frequency domain corroborate this description, as shown in Fig. 2(b). At 9.2 and 14.1 T, there is a single peak observed, whose center frequency increases with the magnetic field. Above 14 T, the peak splits into two, and the splitting magnitude increases with increasing magnetic field.

To understand our experimental data quantitatively, we developed a microscopic theoretical model. Complete derivations are reported in the Supplemental Material [36]. First, we derive the relative permeability in the  $c$ -cut crystal configuration, following the Herrmann model [34]. We consider two sublattices with spins  $\vec{S}_1$  and  $\vec{S}_2$ , as depicted in Figs. 1(b) and 1(c). The free energy of this system is given by

$$V = E\vec{S}_1 \cdot \vec{S}_2 - D(S_{1x}S_{2z} - S_{2x}S_{1z}) - A_{xx}(S_{1x}^2 + S_{2x}^2) - A_{zz}(S_{1z}^2 + S_{2z}^2) - \mu_0\vec{H}_{\text{dc}} \cdot (\vec{S}_1 + \vec{S}_2), \quad (1)$$

which contains the isotropic exchange interaction (the first term with coefficient  $E$ ), the Dzyaloshinskii-Moriya interaction (the second term with coefficient  $D$ ), the anisotropy energies (the third and fourth terms with coefficients  $A_{xx}$  and  $A_{zz}$ , respectively), and the Zeeman interaction with the external dc magnetic field (the last term);  $\mu_0$  is the vacuum permeability.

The equation of motion for the  $i$ th component of the spins can be written as

$$\frac{1}{\gamma_r}\dot{\vec{R}}_i = \vec{R}_i \times \nabla_i V - \frac{\alpha}{\gamma_r}\vec{R}_i \times \dot{\vec{R}}_i, \quad (2)$$

where  $\vec{R}_i = \vec{S}_i/|\vec{S}_i|$  are the normalized spins with  $|\vec{S}_i| = 5/2$ ,  $\gamma_r$  is the gyromagnetic ratio, and  $\alpha$  is the dimensionless Gilbert damping coefficient. By solving Eq. (2) with the free energy  $V$  given by Eq. (1), we can obtain the resonance frequency,  $\omega_0$ , and the magnetic susceptibility tensor for the qFM and qAFM modes without any fitting parameters. Because the THz magnetic field is along the  $a$  axis, we focus on the  $xx$  element of the magnetic susceptibility tensor,

$$\chi_{xx} = \frac{\Delta\mu_{xx}}{\omega_0^2 - \omega^2 - i\omega\gamma} \omega_0^2, \quad \Delta\mu_{xx} \propto \frac{\langle R_{1z} + R_{2z} \rangle^2}{\omega_0^2}, \quad (3)$$

where  $\gamma$  is the matter decay rate, which includes Gilbert damping and interactions. All necessary physical quantities are taken from the literature (see Supplemental Material [36]).

Next, we calculated THz transmittance spectra by the scattering matrix method using the relative permeability obtained from the microscopic model (see Supplemental Material [36]) and deduced the resonance frequencies. Figure 3(a) summarizes the frequencies ( $\omega$ ) of the peaks normalized by the

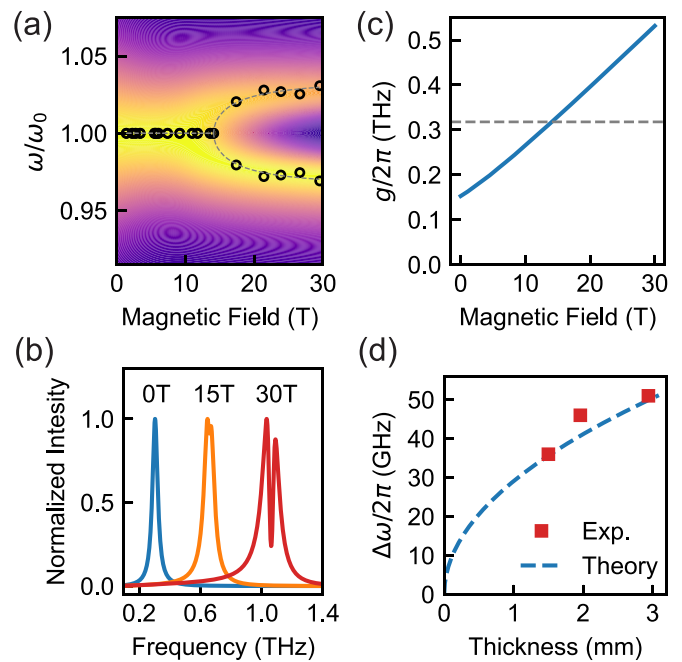


FIG. 3. (a) The frequency  $\omega$  of the qFM mode, normalized by the center frequency  $\omega_0$ , as a function of magnetic field. At high fields, the qFM resonance splits into two, which is attributed to the formation of a bulk magnon polariton. The color map is our simulated spectra. The open circles are obtained from experimental data, and the dashed lines are square-root function fits. (b) Calculated magnon polariton spectra for three values of magnetic field—0, 15, and 30 T. (c) Calculated coupling strength  $g$  as a function of magnetic field. The dashed line indicates the loss  $\sqrt{\kappa\gamma}/2$ . (d) The magnitude of splitting  $\Delta\omega$  versus sample thickness.

center magnon frequency ( $\omega_0$ ) determined both from the experiment and the calculation. The numerical data is presented as a color map, while open circles indicate the experimental data. Dashed lines are square-root fits. Figure 3(b) shows theoretical traces at 0 T, 15 T, and 30 T obtained from the color map in Fig. 3(a). Theory and experimental data are in good agreement. As the applied magnetic field increases, the splitting between the two peaks increases. The transition from weak coupling to strong coupling occurs through the exceptional point (a spectral singularity where the eigenvalues and eigenvectors coalesce [18]).

Here, the eigenvalues are the complex frequencies  $\omega_{\pm}$  that satisfy Eq. (26) of the Supplemental Material [36]. The eigenvectors are the electric field  $(E_x, E_y)^T$  with components in the  $x$  and  $y$  directions. Our system shows the conservative-type coupling, where the two complex eigenfrequencies form a real-valued coupling strength. Thus, opposite to the case of dissipative coupling [29], the two peaks do not collapse again with further increasing magnetic field, but the gap monotonically increases as plotted by the gray dashed line in Fig. 3(a) due to the real-valued coupling strength. The abrupt aspect of the exceptional point seen in Fig. 3(a) occurs when the coupling strength equals losses in the system (see Supplemental Material [36]).

The dependence of the splitting on the magnetic field can be explained by the magnetic field dependence of the effective

oscillator strength,  $\Delta\mu_{xx}$ . For the case of scalar susceptibility and zero damping it can be shown (see Supplemental Material [36]) that the frequency splitting,  $\Delta\omega$ , depends on the effective oscillator strength,  $\Delta\mu_{xx}$  as

$$\Delta\omega = \omega_0 \sqrt{\Delta\mu_{xx}}. \quad (4)$$

We see that the effective oscillator strength and magnon frequency contribute to the frequency splitting of the magnon-polariton. Equation (3) shows that  $\Delta\mu_{xx}$  depends on the average of the  $z$  components of the two spins  $\langle R_{1z} + R_{2z} \rangle$ , which increases continuously with increasing magnetic field applied along the  $z$  axis. Thus, the frequency splitting increases with magnetic field.

With further theoretical analysis, we can obtain the light-matter coupling strength,  $g$ , as a function of the magnetic field, which is plotted in Fig. 3(c), where the dashed line indicates the light and matter losses,  $\sqrt{\kappa\gamma}/2$ . The existence of an exceptional point can be naturally explained as the competition between the matter dissipation rate ( $\gamma$ ) and light effective loss rate ( $\kappa$ ), which are independent of the magnetic field, and the light-matter coupling strength ( $g$ ), which increases with the field. At low magnetic fields, the dissipation wins, while at high magnetic fields, the coupling wins. Thus, in this system, the external magnetic field induces an *in situ* continuous transition between the weak-coupling regime (at low fields) and the strong-coupling regime (at high fields). At the exceptional point (14 T), the loss and the coupling strength are equal. Therefore, the effective loss rate of light can be calculated  $\kappa = 11$  THz with  $\gamma = 0.035$  THz. Such relatively high effective loss rate (escape rate) of light reflects the absence of the cavity structure.

Finally, we also found that the magnitude of splitting also increases with the sample thickness,  $d$  [see Fig. 3(d)]. A similar splitting of THz magnon polaritons has been previously observed as a function of temperature at zero magnetic field [37,38], but only qualitative explanations were given. Here, we demonstrated that the splitting shows a  $\sqrt{d}$  dependence at a fixed magnetic field, as shown in Fig. 3(d). The dashed line, which is proportional to  $\sqrt{d}$ , was obtained from calculations using our microscopic model (see Supplemental Material [36]), as detailed below, and agrees well with the experimental data. The coupling strength,  $g$ , is known to be proportional to the density of two-level objects,  $\rho$ , i.e.,  $g \propto \sqrt{\rho}$  [8,39,40]. Usually, such a dependence is discussed in the context of

light-matter coupling in a cavity [41,42], where the volume is kept constant, and the density dependence is replaced with the dependence on the number of spins,  $g \propto \sqrt{N}$  [24,39,43,44]. In our case, this cannot be true, as the density of spins is constant as a function of thickness. However, the splitting as a function of thickness also follows the square-root dependence,  $\Delta\omega \propto \sqrt{d}$ , as summarized in Fig. 3(d). Such behavior instead can be understood as arising from the boundary conditions of Maxwell equations for the THz wave propagation, similar to exciton-polaritons in a finite system [45].

In conclusion, we investigated YFeO<sub>3</sub> crystals with different thicknesses using single-shot THz time-domain spectroscopy in high magnetic fields up to 30 T. We observed that above about 14 T the quasiferromagnetic magnon mode splits into two peaks and the frequency splitting keeps increasing with increasing magnetic field. This behavior can be explained by the formation of bulk magnon polaritons. Our theoretical model based on the microscopic permeability tensor and scattering matrix method agrees well with the experimental data. From the model, it follows that the frequency splitting dependence on magnetic fields arises from the dependence of the effective oscillator strength on the magnetic field. Furthermore, we show that the coupling strength can be continuously tuned by the applied magnetic field. Thus, our results demonstrate that the strong photon-magnon coupling can be controlled by the magnetic field. This adds bulk THz magnon polaritons in antiferromagnets to other systems supporting exceptional points, which are promising for further exploration of non-Hermitian physics and advanced sensing.

J.K. acknowledges support from the U.S. Army Research Office (Grant No. W911NF2110157), W. M. Keck Foundation (Grant No. 995764), and the Robert A. Welch Foundation (Grant No. C-1509). This research was partially supported by the National Science Foundation through the Center for Dynamics and Control of Materials: an NSF MRSEC under Cooperative Agreement No. DMR-1720595. M.B. acknowledges support from the JST PRESTO program (Grant No. JPMJPR1767). J.T. and I.K. acknowledge the support from the Japan Society for the Promotion of Science (JSPS) (KAKENHI Grant No. 20H05662). S.C., W.R., and G.M. are grateful for financial support from the National Natural Science Foundation of China (NSFC, Grant No.12074242) and the Science and Technology Commission of Shanghai Municipality (Grant No. 21JC1402600).

[1] F. Verstraete, M. M. Wolf, and J. Ignacio Cirac, Quantum computation and quantum-state engineering driven by dissipation, *Nat. Phys.* **5**, 633 (2009).  
 [2] R. Schmidt, A. Negretti, J. Ankerhold, T. Calarco, and J. T. Stockburger, Optimal Control of Open Quantum Systems: Cooperative Effects of Driving and Dissipation, *Phys. Rev. Lett.* **107**, 130404 (2011).  
 [3] F. Reiter, A. S. Sørensen, P. Zoller, and C. A. Muschik, Dissipative quantum error correction and application to quantum sensing with trapped ions, *Nat. Commun.* **8**, 1822 (2017).

[4] S. Touzard, A. Grimm, Z. Leghtas, S. O. Mundhada, P. Reinhold, C. Axline, M. Reagor, K. Chou, J. Blumoff, K. M. Sliwa, S. Shankar, L. Frunzio, R. J. Schoelkopf, M. Mirrahimi, and M. H. Devoret, Coherent Oscillations Inside a Quantum Manifold Stabilized by Dissipation, *Phys. Rev. X* **8**, 021005 (2018).  
 [5] M. J. Hartmann, F. G. S. L. Brandão, and M. B. Plenio, Strongly interacting polaritons in coupled arrays of cavities, *Nat. Phys.* **2**, 849 (2006).  
 [6] M. Foss-Feig, J. T. Young, V. V. Albert, A. V. Gorshkov, and M. F. Maghrebi, Solvable Family of Driven-Dissipative



- Many-Body Systems, *Phys. Rev. Lett.* **119**, 190402 (2017).
- [7] R. Ma, B. Saxberg, C. Owens, N. Leung, Y. Lu, J. Simon, and D. I. Schuster, A dissipatively stabilized Mott insulator of photons, *Nature (London)* **566**, 51 (2019).
- [8] N. M. Peraca, A. Baydin, W. Gao, M. Bamba, and J. Kono, Ultrastrong light–matter coupling in semiconductors, in *Semiconductors and Semimetals* (Elsevier, New York, 2020), Vol. 105, pp. 89–151.
- [9] P. Forn-Díaz, L. Lamata, E. Rico, J. Kono, and E. Solano, Ultrastrong coupling regimes of light–matter interaction, *Rev. Mod. Phys.* **91**, 025005 (2019).
- [10] A. F. Kockum, A. Miranowicz, S. De Liberato, S. Savasta, and F. Nori, Ultrastrong coupling between light and matter, *Nat. Rev. Phys.* **1**, 19 (2019).
- [11] F. Quijandría, U. Naether, S. K. Özdemir, F. Nori, and D. Zueco,  $\mathcal{PT}$ -symmetric circuit QED, *Phys. Rev. A* **97**, 053846 (2018).
- [12] Y.-W. Lu, J.-F. Liu, R. Liu, R. Su, and X.-H. Wang, Quantum exceptional chamber induced by large nondipole effect of a quantum dot coupled to a nano-plasmonic resonator, *Nanophotonics* **10**, 2431 (2021).
- [13] F. Minganti, A. Miranowicz, R. W. Chhajlany, and F. Nori, Quantum exceptional points of non-Hermitian Hamiltonians and Liouvillians: The effects of quantum jumps, *Phys. Rev. A* **100**, 062131 (2019).
- [14] J. Huber, P. Kirton, S. Rotter, and P. Rabl, Emergence of  $\mathcal{PT}$ -symmetry breaking in open quantum systems, *SciPost Phys.* **9**, 052 (2020).
- [15] I. I. Arkhipov, F. Minganti, A. Miranowicz, and F. Nori, Generating high-order quantum exceptional points in synthetic dimensions, *Phys. Rev. A* **104**, 012205 (2021).
- [16] A. Purkayastha, M. Kulkarni, and Y. N. Joglekar, Emergent  $\mathcal{PT}$  symmetry in a double-quantum-dot circuit QED setup, *Phys. Rev. Res.* **2**, 043075 (2020).
- [17] D. Xie, C. Xu, and A. M. Wang, Parameter estimation and quantum entanglement in  $\mathcal{PT}$  symmetrical cavity magnonics system, *Results Phys.* **26**, 104430 (2021).
- [18] W. D. Heiss, The physics of exceptional points, *J. Phys. A: Math. Theor.* **45**, 444016 (2012).
- [19] M.-A. Miri and A. Alù, Exceptional points in optics and photonics, *Science* **363**, eaar7709 (2019).
- [20] Ş. K. Özdemir, S. Rotter, F. Nori, and L. Yang, Parity–time symmetry and exceptional points in photonics, *Nat. Mater.* **18**, 783 (2019).
- [21] Y. Ashida, Z. Gong, and M. Ueda, Non-Hermitian physics, *Adv. Phys.* **69**, 249 (2020).
- [22] A. A. Anappara, A. Tredicucci, G. Biasiol, and L. Sorba, Electrical control of polariton coupling in intersubband microcavities, *Appl. Phys. Lett.* **87**, 051105 (2005).
- [23] G. Günter, A. A. Anappara, J. Hees, A. Sell, G. Biasiol, L. Sorba, S. De Liberato, C. Ciuti, A. Tredicucci, A. Leitenstorfer, and R. Huber, Sub-cycle switch-on of ultrastrong light–matter interaction, *Nature (London)* **458**, 178 (2009).
- [24] W. Gao, X. Li, M. Bamba, and J. Kono, Continuous transition between weak and ultrastrong coupling through exceptional points in carbon nanotube microcavity exciton–polaritons, *Nat. Photon.* **12**, 362 (2018).
- [25] C. F. Doiron and G. V. Naik, Non-Hermitian selective thermal emitters using metal–semiconductor hybrid resonators, *Adv. Mater.* **31**, 1904154 (2019).
- [26] D. Zhang, X.-Q. Luo, Y.-P. Wang, T.-F. Li, and J. Q. You, Observation of the exceptional point in cavity magnon-polaritons, *Nat. Commun.* **8**, 1368 (2017).
- [27] X. Zhang, K. Ding, X. Zhou, J. Xu, and D. Jin, Experimental Observation of an Exceptional Surface in Synthetic Dimensions with Magnon Polaritons, *Phys. Rev. Lett.* **123**, 237202 (2019).
- [28] I. Boventer, C. Dörrflinger, T. Wolz, R. Macêdo, R. Lebrun, M. Kläui, and M. Weides, Control of the coupling strength and linewidth of a cavity magnon-polariton, *Phys. Rev. Res.* **2**, 013154 (2020).
- [29] Y.-P. Wang and C.-M. Hu, Dissipative couplings in cavity magnonics, *J. Appl. Phys.* **127**, 130901 (2020).
- [30] M. Harder, B. M. Yao, Y. S. Gui, and C.-M. Hu, Coherent and dissipative cavity magnonics, *J. Appl. Phys.* **129**, 201101 (2021).
- [31] G. T. Noe II, I. Katayama, F. Katsutani, J. J. Allred, J. A. Horowitz, D. M. Sullivan, Q. Zhang, F. Sekiguchi, G. L. Woods, M. C. Hoffmann, H. Nojiri, J. Takeda, and J. Kono, Single-shot terahertz time-domain spectroscopy in pulsed high magnetic fields, *Opt. Express* **24**, 30328 (2016).
- [32] A. Baydin, T. Makihara, N. M. Peraca, and J. Kono, Time-domain terahertz spectroscopy in high magnetic fields, *Front. Optoelectron.* **14**, 110 (2021).
- [33] F. Tay, A. Baydin, F. Katsutani, and J. Kono, Magneto-optical spectroscopy with RAMBO: A table-top 30 T magnet, *J. Phys. Soc. Jpn.* **91**, 101006 (2022).
- [34] G. Herrmann, Resonance and high frequency susceptibility in canted antiferromagnetic substances, *J. Phys. Chem. Solids* **24**, 597 (1963).
- [35] T. Makihara, K. Hayashida, G. T. Noe II, X. Li, N. Marquez Peraca, X. Ma, Z. Jin, W. Ren, G. Ma, I. Katayama, J. Takeda, H. Nojiri, D. Turchinovich, S. Cao, M. Bamba, and J. Kono, Ultrastrong magnon–magnon coupling dominated by antiresonant interactions, *Nat. Commun.* **12**, 3115 (2021).
- [36] See Supplemental Material at <http://link.aps.org/supplemental/10.1103/PhysRevResearch.5.L012039> for details on the microscopic theory for bulk magnon polaritons.
- [37] K. Grishunin, T. Huisman, G. Li, E. Mishina, T. Rasing, A. V. Kimel, K. Zhang, Z. Jin, S. Cao, W. Ren, G.-H. Ma, and R. V. Mikhaylovskiy, Terahertz magnon-polaritons in  $\text{TmFeO}_3$ , *ACS Photon.* **5**, 1375 (2018).
- [38] L. Y. Shi, D. Wu, Z. X. Wang, T. Lin, C. M. Hu, and N. L. Wang, Revealing strong magnon-photon coupling in a polar antiferromagnet  $\text{Fe}_2\text{Mo}_3\text{O}_8$  by time domain terahertz spectroscopy, [arXiv:2004.05823](https://arxiv.org/abs/2004.05823).
- [39] X. Li, M. Bamba, N. Yuan, Q. Zhang, Y. Zhao, M. Xiang, K. Xu, Z. Jin, W. Ren, G. Ma, S. Cao, D. Turchinovich, and J. Kono, Observation of Dicke cooperativity in magnetic interactions, *Science* **361**, 794 (2018).
- [40] Q. Zhang, M. Lou, X. Li, J. L. Reno, W. Pan, J. D. Watson, M. J. Manfra, and J. Kono, Collective non-perturbative coupling of 2D electrons with high-quality-factor terahertz cavity photons, *Nat. Phys.* **12**, 1005 (2016).
- [41] H. Huebl, C. W. Zollitsch, J. Lotze, F. Hocke, M. Greifenstein, A. Marx, R. Gross, and S. T. B. Goennenwein, High Cooperativity in Coupled Microwave Resonator Ferrimagnetic Insulator Hybrids, *Phys. Rev. Lett.* **111**, 127003 (2013).
- [42] H. Y. Yuan and X. R. Wang, Magnon-photon coupling in antiferromagnets, *Appl. Phys. Lett.* **110**, 082403 (2017).

- [43] R. H. Dicke, Coherence in Spontaneous Radiation Processes, *Phys. Rev.* **93**, 99 (1954).
- [44] R. Yahiaoui, Z. A. Chase, C. Kyaw, F. Tay, A. Baydin, G. T. Noe II, J. Kono, J. Seo, A. Agrawal, M. Bamba, and T. A. Searles, Dicke-cooperativity-assisted ultrastrong coupling enhancement in terahertz metasurfaces, *Nano Letters* **24**, 9788 (2022).
- [45] M. Bamba and H. Ishihara, Crossover of exciton-photon coupled modes in a finite system, *Phys. Rev. B* **80**, 125319 (2009).